Batteries & Supercaps

Research Article
doi.org/10.1002/batt.202500524

Chemistry Europe
European Chemical
Societies Publishing

www.batteries-supercaps.org

Design and Application of Hydrogen-Bonded Organic Frameworks with Tetrathiafulvalene-Tetrabenzoate for Cathode Active Materials in Lithium- and Sodium-Ion Batteries

Katsuhiro Wakamatsu,* Soichiro Furuno, Hosei Oshima, Naoki Kobayashi, Tomohiro Miyaji, Takeshi Shimizu, Heng Wang, and Hirofumi Yoshikawa*

Hydrogen-bonded organic frameworks (HOFs) have been increasingly applied in industrial fields owing to their low weight and high pore volume. In particular, HOFs incorporating redox-active units have emerged as promising electrode materials for energy storage devices alongside other porous organic polymers. This study explores the application of HOFs incorporating tetrathiafulvalene (TTF) derivatives that are well-known as molecular conductors with multielectron redox properties for rechargeable batteries. Specifically, the battery performance of HOFs-based TTF-tetrabenzoate (H_4TTFTB) as a cathode active material in lithium-ion (LIBs) and sodium-ion batteries (SIBs) is evaluated. H_4TTFTB-based HOFs demonstrate enhanced cycling stability, with a particularly large enhancement achieved in SIB systems, due to the inherent structural stability of HOFs. Additionally, driven by the synergistic redox activity of TTF and bipyridine units, TTF-hybrid-HOFs combining H_4TTFTB with redox-active bipyridine units exhibit improved battery capacities. These findings underscore the potential of H_4TTFTB-based HOFs, which combine excellent redox activity and mechanical stability, as promising candidates for high-performance energy storage devices, highlighting the advantages of integrating rigid heterocyclic compounds with redox-active functionalities into HOF structures for future battery applications.

1. Introduction

The increasing demand for sustainable energy solutions, driven by concerns over fossil fuel depletion and global warming, underscores the urgent need for high-efficiency, high-output, and high-energy-density energy storage technologies.[1] Lithium-ion batteries (LIBs) and sodium-ion batteries (SIBs) have emerged as key technologies for decarbonization in the transportation and energy sectors. LIBs are widely used due to their high energy density and performance,[2] while SIBs offer a cost-effective alternative technology that benefits from the natural abundance of sodium[3] and shares similar electrochemical mechanisms with LIBs.[4] Despite their promise, both LIBs and SIBs face critical challenges. The rising cost of transition–metal-based materials[5] and performance issues such as low cycling stability and limited energy density often caused by degradation of active materials[6–8] hinder further progress in the development of LIBs and SIBs. In particular, SIBs typically exhibit lower energy density due to reduced operating voltages[8] and the larger ionic radius and less efficient redox chemistry of Na^+ compared to $Li^{+[9]}$. Nevertheless, LIBs and SIBs are expected to dominate energy storage markets,[2] and innovations that enhance their performance are vital for meeting future energy demand.[10]

The use of organic compounds as cathode active materials is a promising strategy for addressing the limitations of LIBs and SIBs. Organic cathodes offer several benefits, including high theoretical capacities, environmental friendliness, and easy availability of constituent elements.[11,12] However, they also suffer from low electrical conductivity, low redox potentials (leading to lower energy density), and poor cycle stability due to their solubility in the battery electrolytes.[12,13] Therefore, the development of redox-active organic materials with high electrical conductivity, elevated redox potentials, and robust structural integrity remains essential.

K. Wakamatsu, S. Furuno, H. Oshima, N. Kobayashi, T. Miyaji,
H. Yoshikawa
Graduate School of Science and Technology
Kwansei Gakuin University
1 Gakuen Uegahara, Sanda, Hyogo 669–1330, Japan
E-mail: guk00031@kwansei.ac.jp
           yoshikawah@kwansei.ac.jp

K. Wakamatsu
Department of Chemical Engineering
Massachusetts Institute of Technology
77 Massachusetts Avenue, Cambridge, Massachusetts 02139, USA

T. Shimizu
Chemistry and Biochemistry Division
Department of Integrated Engineering
National Institute of Technology
Yonago College
4448 Hikona-cho, Yonago, Tottori 683–8502, Japan

H. Wang
College of New Energy
Zhengzhou University of Light Industry
136 Ke Xue Avenue, Zhengzhou, Henan 450000, China

Among the various redox-active molecules, tetrathiafulvene (TTF) has garnered significant attention. TTF is a π-conjugated, sulfur-rich, electron-donating molecule with 14 π-electrons.[14,15] Owing to its structural versatility and redox-active nature, TTF has been extensively incorporated into a wide range of molecular and supramolecular architectures.[16] Its unique electronic configuration enables stable and reversible two-electron redox behavior at relatively high potentials via a P-type redox mechanism,[17–22] as illustrated in **Figure 1** and **2**a. TTF derivatives have been utilized in various industrial applications, including as conductive,[23,24] magnetic,[25–27] and catalytic materials,[28,29] as well as in optoelectronic devices.[30,31] In particular, TTF has emerged as a promising candidate for use as an electrode material in rechargeable batteries, owing to its high redox potential and the resulting high energy density derived from its P-type redox characteristics. While most reported organic electrode materials for rechargeable batteries exhibit N-type redox behavior,[21] wherein cations are inserted upon reduction, applications of P-type materials remain relatively limited.[21] In this context, TTF stands out due to its P-type redox mechanism, which facilitates redox activity at higher potentials and thus is highly promising for the development of high-performance rechargeable batteries. During the P-type redox process of TTF, electrons are extracted from the redox-active molecule during the charging process, forming positively charged species. These positive charges are compensated by the insertion of counter anions, such as PF_6^- and ClO_4^-, from the electrolyte into the cathode, accompanied by metal ion deposition at the anode. Conversely, during the discharging process, electrons are reintroduced to the system, leading to the reduction of the TTF units and the formation of neutral species.[22] This is accompanied by the extraction (deinsertion) of the counter anions from the cathode and dissolution of metal ions at the anode (Figure 1).

The utility of TTF in rechargeable batteries has also been demonstrated. For example, Misaki et al. reported a TTF derivative, tetrakis(methylthio) derivative ($C_{38}H_{24}S_{24}$), with a 10-electron redox process and excellent cycling stability when used as a cathode in LIBs.[32] In addition, Yuansheng et al. synthesized BDTTS by introducing carboxylic acid groups at the terminal positions of the TTF molecule and demonstrated improved cycling stability when used as an anode material in SIBs.[33] These studies indicate that both polymerization strategies and molecular modifications are effective in suppressing the dissolution of TTF-based molecules into the electrolyte,[32–34] thereby highlighting the high potential of TTF-based systems for high-performance organic electrodes.[20,32–37] Building on these properties, TTF-based porous frameworks, such as metal–organic frameworks (MOFs) and covalent organic frameworks (COFs), have emerged as attractive materials for energy storage due to their high surface areas, structural tunability, porosity, and the possibility of introducing functional groups to increase ion adsorption sites and modulate electronic states, thereby enhancing redox activity and conductivity.[38–42] For instance, Yi-Gang et al. employed Zn- and Co-based MOFs with 2,6-bis(4′-pyridyl)tetrathiafulvalene (py-TTF-py) ligands as anode materias,[15] and Wen et al. reported that Zr-MOFs incorporating tetrathiafulvalene-tetrabenzoate (H_4TTFTB, Figure S1a, Supporting Information) or its methylated derivatives have been shown to be promising for use as hybrid capacitive anodes.[33] Similarly, Zhi-Mei et al. achieved excellent anode performance in a TTF-based COF (TTFTTA-PDA-COF) incorporating thiophene units, which was attributed to the advantageous redox characteristics of the TTF core.[43] Our prior work
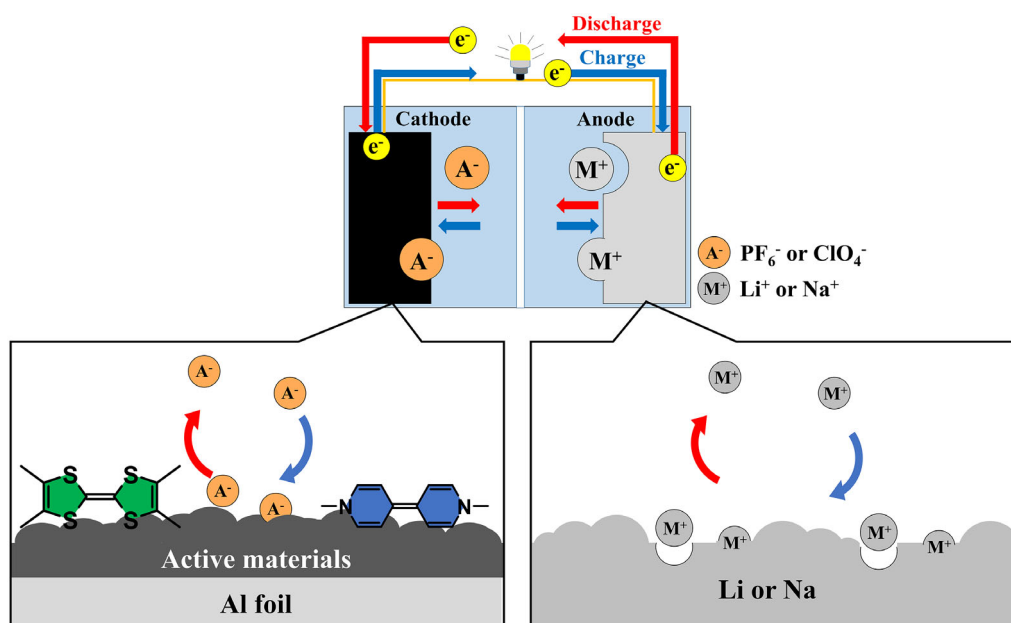

Figure 1. Schematic illustration of the charge–discharge mechanism of the rechargeable battery using TTF (green) and bipyridine (blue) units as active materials. Here, A and M represent PF_6^- or ClO_4^-, and Li^+ or Na^+, respectively.

Batteries & Supercaps

Research Article
doi.org/10.1002/batt.202500524

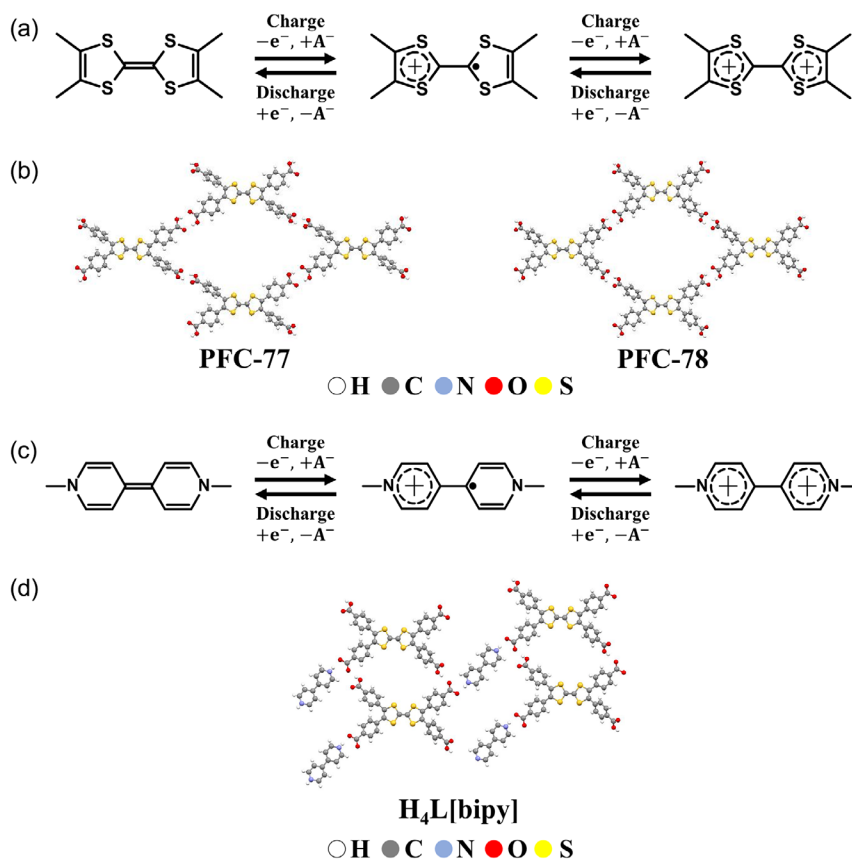**Chemistry Europe**
European Chemical
Societies Publishing

Figure 2. a) Redox reactions occurring in the TTF units of PFC-77, PFC-78, and H$_4$L[bipy], b) schematic structures of PFC-77 and PFC-78, c) redox reaction occurring in the bipyridine units of H$_4$L[bipy], and d) schematic structure of H$_4$L[bipy]. Here, A represents PF$_6^-$ or ClO$_4^-$, and atoms are color-coded: white (H), gray (C), blue (N), red (O), and yellow (S).

extended this approach to the Zn$_2$(TTFTB), Co$_2$(TTFTB), and Mn$_2$(TTFTB) TTF-based MOFs which demonstrated enhanced cycling stability and improved capacity even under high current densities when used as cathode materials for LIBs and SIBs.[44]

Recently, hydrogen-bonded organic frameworks (HOFs) have emerged as a new class of materials for battery electrodes. Constructed entirely from organic molecules held together by hydrogen bonds, HOFs are lightweight, environmentally friendly, and easy to process via recrystallization.[45] These features make them attractive for cathodes in rechargeable battery applications. For example, Hisaki et al. reported a nitrogen-rich HOF (hexaaza-trinaphthylene (HATN) derivatives with carboxyphenyl groups, CPHATN-1a) with a six-electron redox process in LIBs,[46] and Guo et al. utilized iodine-loaded PFC-1 (I$_2$/HOF) for Li–I$_2$ batteries.[47] Wasielewski et al. have explored guanine–diimide HOFs (G2PDI) in LIBs[48] and imide-containing HOFs (diaminotriazole, DAT) for SIBs were reported by Wu et al.[49] achieving high current performance. In our previous work, we demonstrated that N,N-bis(2-isophthalic acid)naphthalenediimide (ECUT-HOF-30) and 4,4′,4″-(1,3,5-triazine-2,4,6-triyl)-tribenzoic acid-based HOFs (PFC-11, PFC-12, and PFC-13, PFC = porous materials from FJIRSM, CAS), which contains imide and triazine units, respectively, can be used effectively in both LIBs and SIBs.[50,51] These examples highlight the potential of HOFs, particularly those incorporating redox-active motifs, in next-generation energy storage. However, the impact of the structural diversity of HOFs on electrochemical performance remains poorly understood.

In this study, we focus on H$_4$TTFTB-based HOFs, specifically PFC-77 and PFC-78,[52] which serve as model systems due to their low molecular weight and redox-active TTF cores with anion deinsertion. Despite sharing the same molecular formula, these HOFs form distinct crystal structures, offering a valuable opportunity to investigate how structural variations influence ion (de)insertion behavior and battery performance (Figure 2a,b and S2a,b, Supporting Information). Additionally, we explore TTF-bipyridine-hybrid-HOFs (H$_4$L[bipy]),[19] shown in Figure 2c and S2c, Supporting Information, which combine TTF units with additional bipyridine redox-active sites (derived from 4,4′-bipyridyl, Figure S1b, Supporting Information). Bipyridine is of particular interest because, similar to TTF, it undergoes P-type redox reactions involving reversible anion insertion and deinsertion[21,53] (Figure 1 and 2c). Furthermore, the heterocyclic structure of bipyridine (nitrogen-containing heterocycles) endows it with high electrochemical and structural stability.[54] This hybrid approach is intended to enhance energy storage performance through multisite redox activity. We evaluated these materials as cathode electrodes for both LIBs and SIBs, comparing their electron storage capacities and electrochemical performance

Batteries & Supercaps

Research Article
doi.org/10.1002/batt.202500524

Chemistry Europe
European Chemical
Societies Publishing

characteristics to those of the H₄TTFTB precursor. Furthermore, we benchmarked their performance against other TTF-based porous materials, including COFs and MOFs, as well as previously reported HOFs. Our findings offer new insights into the structure–function relationships of TTF-based HOFs and demonstrate their potential as advanced materials for high-performance recharge-able batteries.

2. Results and Discussion

2.1. Electrochemical Behavior of TTF-Based HOF Cathodes in LIB Systems

We investigated the battery performance of PFC-77 and PFC-78, which incorporate redox-active TTF units, as well as H₄L[bipy], which incorporate redox-active TTF and bipyridine units, as cathode active materials for rechargeable LIBs and SIBs. We seek to explore the benefits of the integration of rigid heterocyclic compounds with redox-active functionalities. Detailed characterization results, including the results of the powder X-ray diffraction (PXRD), Fourier transform infrared (FTIR) spectroscopy, scanning electron microscopy (SEM), and nitrogen gas adsorption/desorption measurements for PFC-77, PFC-78, and H₄L[bipy] are provided in the Supporting Information (Figure S3a–c, S4a,b, S5a–c, S6a–e, and S7a–c, Supporting Information).

The charge–discharge profiles of PFC-77, PFC-78, and H₄L[bipy], along with that of H₄TTFTB, measured at a current density of 100 mA g^{-1} in LIBs, are presented in **Figure 3**a,c,e, and S8a, Supporting Information, respectively. Figure 3g shows the cycle dependence of the discharge capacities and the Coulombic efficiencies for PFC-77, PFC-78, H₄L[bipy], and H₄TTFTB at a current density of 100 mA g^{-1} in LIBs. In this study, the charging process was initiated. During the initial charging process, two distinct plateaus were observed at ≈3.4–4.0 V. Moreover, two different plateaus were also observed at ≈3.0–3.6 V during the initial discharge process. The observed charge–discharge plateaus closely matched those previously reported for TTF units[21,36,55,56] (charge: 3.6 and 3.8 V[55]; discharge: 3.1 and 3.5 V[21,55]), indicating that the redox behavior of our TTF units is consistent with the known TTF characteristics. Additionally, gentle two-step plateaus were observed at ≈2.0–2.5 V in the initial discharge profile of H₄L[bipy], and a gentle, slight two-step charge plateau was observed at ≈2.0–2.6 V. This feature is likely to be due to the redox activity of the bipyridine units,[56–58] consistent with the previous reports on LIBs incorporating bipyridine functionalities which exhibited charge/discharge plateaus at ≈2.1 and 2.6 V during charging[57] and at 2.1 and 2.4 V during discharging.[56] As shown in Figure S8b, Supporting Information, similar discharge plateaus were observed in LIBs for the skeletal molecular units containing the 4,4′-bipyridyl bipyridine group, consistent with the bipyridine-derived charge/discharge behavior observed in the hybrid TTF-HOFs investigated in this study. Additionally, early studies reported that in LIBs, carboxylic groups can undergo irreversible redox reactions during discharge at around 1.5 V as previously repoted, resulting in the transformation to –COOLi and
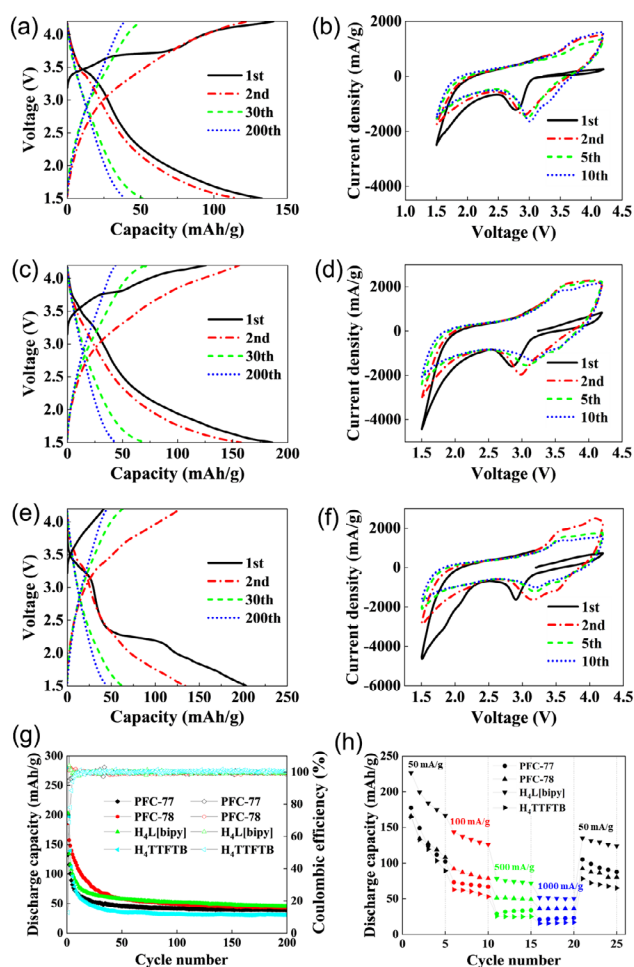

Figure 3. a) Discharge/charge curves of PFC-77 at a current density of 100 mA g^{-1} in LIBs. b) CV profiles of PFC-77 in LIBs. c) Discharge/charge curves of PFC-78 at a current density of 100 mA g^{-1} in LIBs. d) CV profiles of PFC-78 in LIBs. e) Discharge/charge curves of H₄L[bipy] at a current density of 100 mA g^{-1} in LIBs. f) CV profiles of H₄L[bipy] in LIBs. g) Discharge capacity and Coulombic efficiency as a function of cycle number for H₄TTFTB, PFC-77, PFC-78, and H₄L[bipy] at a current density of 100 mA g^{-1} in LIBs. Filled symbols represent discharge capacity, while unfilled symbols indicate Coulombic efficiency. h) Rate performance of H₄TTFTB, PFC-77, PFC-78, and H₄L[bipy] in LIBs.

subsequent collapse of the framework.[59,60] This can also lead to the formation of a solid–electrolyte interphase (SEI) layer derived from carboxylates, increasing interfacial resistance and contributing to performance decay.[61] It is considered that these reactions are likely occurring in our system as well, where partial disruption of the hydrogen bonds forming the HOF structure may lead to capacity fading over repeated cycles. The Coulombic efficiency remained stable at ≈100% over 200 cycles for all tested materials, as shown in Figure 3g, highlighting their robust and consistent redox properties.

Table 1 summarizes the key battery performance metrics for PFC-77, PFC-78, H₄L[bipy], and H₄TTFTB in LIBs at a current density of 100 mA g^{-1}. The metrics include the maximum discharge capacity within the initial five cycles, discharge capacity in the 30th cycle at which the capacity is stabilized following its initial

© 2025 Wiley-VCH GmbH

Batteries & Supercaps

Research Article
doi.org/10.1002/batt.202500524

Chemistry Europe
European Chemical
Societies Publishing

Table 1. Maximum, 30th cycle, and 200th cycle discharge capacities, along with capacity retention rates after 200 cycles for H_4TTFTB, PFC-77, PFC-78, and $H_4L[bipy]$ at a current density of 100 mA g^{-1} in LIBs. Note that all maximum capacities occur at the first cycle. Discharge capacity retention rates are calculated as the discharge capacity after the 200th cycle divided by the discharge capacity after the 30th cycle at which the capacity is stabilized following its initial decrease.

Materials	LIBs			
	Maximum [mAh g^{-1}]	30th cycle [mAh g^{-1}]	200th cycle [mAh g^{-1}]	Retention rates [%]
PFC-77	133	51	39	77
PFC-78	186	70	44	62
$H_4L[bipy]$	203	62	45	73
H_4TTFTB	279	42	31	74

decrease, discharge capacity after the 200th cycle, and the corresponding capacity retention rates. The maximum discharge capacities during the initial cycle for PFC-77, PFC-78, $H_4L[bipy]$, and H_4TTFTB were 133, 186, 203, 192, and 279 mAh g^{-1}, respectively. In the 30th cycle, at which the capacity is stabilized following its initial decrease, the discharge capacities were 51, 70, 62, 88, and 42 mAh g^{-1} for PFC-77, PFC-78, $H_4L[bipy]$, and H_4TTFTB, respectively. Assuming a two-electron redox process per molecular formula driven by the TTF units, the theoretical capacities of PFC-77, PFC-78, and H_4TTFTB are ≈ 78.28 mAh g^{-1} (or 39.14 mAh g^{-1} for a one-electron redox process), as summarized in Table S1, Supporting Information. By contrast, the theoretical capacity of $H_4L[bipy]$, based on a four-electron redox process per molecular formula arising from both TTF and bipyridine units, is ≈ 124.80 mAh g^{-1}, respectively (31.20 mAh g^{-1}, respectively, for a one-electron redox process), as also summarized in Table S1, Supporting Information. This suggests that in the 30th discharge cycle, the molecular units in PFC-77, PFC-78, $H_4L[bipy]$, and H_4TTFTB undergo redox processes involving 1.31, 1.78, 1.99, and 1.07 electrons, respectively. At the 30th cycle, PFC-77, PFC-78, and H_4TTFTB exhibited an average redox process corresponding to ≈ 1.3 electrons per molecule, while $H_4L[bipy]$ demonstrated higher redox activity, ≈ 2.0 electrons per molecule. In PFC-77, PFC-78, and H_4TTFTB, the redox process primarily arises from the electrochemical activity of the TTF units.[21,55,56] For $H_4L[bipy]$, the presence of both TTF and bipyridine units[56–58] enables additional redox processes, resulting in a higher number of electrons participating in the overall process. While a substantial initial irreversible capacity loss is observed, such behavior is consistent with previously reported results for TTF-based polymers, even when higher contents of active materials are used.[37,62–64] This reinforces that the observed behavior in our study is not unusual for this class of materials. We also consider that part of the initial irreversible capacity may arise from side reactions including the formation of an SEI layer.[36,65]

The cyclic voltammetry (CV) profiles of PFC-77, PFC-78, and $H_4L[bipy]$ in LIBs are presented in Figure 3b,d,f, while those of H_4TTFTB are shown in Figure S9a, Supporting Information. Two-step small sharp peaks were observed at ≈ 3.4–4.0 V during the charging process, while two-step corresponding peaks

appeared at ≈ 3.0–3.6 V during the discharging process. These features closely align with the voltage plateaus observed at 3.4–4.0 and 3.0–3.6 V during the charging and discharging processes, respectively, as shown in Figure 3a,c,e, and S8a, Supporting Information. This consistency indicates that the reversible redox processes of the TTF units occur within the same voltage range as those reported in previous studies (charge: 3.6 and 3.8 V,[55] discharge: 3.1 and 3.5 V[21,36]). In addition, two-step small sharp peaks appeared at ≈ 1.8–2.2 V during the discharge process for $H_4L[bipy]$, although no peak was visible during the charging process. These peaks correspond well to the discharge plateaus in the same voltage range, as shown in Figure 3e, suggesting that redox processes involving bipyridine groups occur within this voltage region (charge: 1.96 and 2.68 V, discharge: 1.94 and 2.44 V).[58] This voltage range is consistent with previously reported values and is considered to be appropriate for battery operation. As shown in Figure S9b, Supporting Information, similar CV peaks were observed for the skeletal molecular units containing the 4,4′-bipyridyl bipyridine group. Notably, the discharge peaks of these molecules correspond closely to the bipyridine-derived discharge peak observed in the hybrid TTF-HOFs in this study. The CV curves from the first cycle, shown in Figure 3b,d,f, exhibit slight deviations from those of the subsequent cycles. This variation is likely due to the pronounced ion intercalation/deintercalation processes and accompanying structural transformations occurring during the initial electrochemical reactions. Moreover, the formation of an SEI layer,[66,67] a well-established phenomenon during the initial cycle, further contributes to the observed differences between the initial and later CV profiles. Such behavior is consistent with prior reports on TTF-based porous polymers, even when higher active material contents are used.[37,63]

The charge–discharge curves, discharge capacity cycling, and Coulombic efficiency, and CV profile of TOKABLACK #5500 at a current density of 50 mA g^{-1} in LIBs are shown in Figure S10a,c,e, Supporting Information. During the initial discharge process, its maximum capacity was ≈ 32.3 mAh g^{-1}, which stabilized at ≈ 25.1 mAh g^{-1} after the capacity decrease in the 30th cycle and the capacity was ≈ 21.7 mAh g^{-1} after the 200th cycle, as shown in Figure S10a,c, Supporting Information. Clear differences are observed in the potential range of 3.0–4.0 (and 1.8–2.5 V) although a minor portion of the observed discharge capacity may be attributed to the capacitive behavior or surface-related processes of the carbon additive. In this region, a distinct discharge plateau appears in the charge–discharge profiles (Figure 3a,c,e and S8a,b, Supporting Information), along with corresponding peaks in the CV curves (Figure 3b,d,f and S9a,b, Supporting Information). These features are absent in the LIBs employing carbon black alone as shown in Figure S10a,e, Supporting Information indicating that they originate from redox activity intrinsic to the TTF (and bipyridine) units in the HOFs. Therefore, the majority of the capacity observed in our system is attributable to the redox reactions of the TTF (and bipyridine) units and the influence of conductive carbon on capacity is limited, even when the active material content is low.

Batteries & Supercaps

Research Article
doi.org/10.1002/batt.202500524

Chemistry
Europe
European Chemical
Societies Publishing

The rate characteristics of PFC-77, PFC-78, H$_4$L[bipy], and H$_4$TTFTB in LIBs are illustrated in Figure 3h. The discharge capacities of all HOFs and H$_4$TTFTB decreased at higher current densities. This reduction is likely due to the inadequate infiltration of Li$^+$ into the pores at the elevated current densities. All HOFs also exhibited higher battery capacities than H$_4$TTFTB, even at elevated current densities in LIBs. This suggests that the porous structure of HOFs has the potential to offer enhanced charging/discharging rates. The electrochemical impedance spectroscopy (EIS) profiles presented in **Figure 4** reveal that for all HOFs, the charge transfer resistances are lower than those of H$_4$TTFTB, suggesting that the formation of HOFs enhances ionic conductivity. This is particularly supported by the presence of pores within the HOF structures, as shown in Figure S2a–c, Supporting Information, because the pores facilitate ion transport, leading to reduced charge transfer resistance.

2.2. Electrochemical Behavior of TTF-Based HOF Cathodes in SIB Systems

The charge–discharge profiles of PFC-77, PFC-78, and H$_4$L[bipy] along with that of H$_4$TTFTB, measured at a current density of 100 mA g^{-1} in SIBs, are shown in **Figure 5**a,c,e, and S8a, Supporting Information, respectively. The cycle dependence of the discharge capacities and Coulombic efficiencies for PFC-77, PFC-78, H$_4$L[bipy], and H$_4$TTFTB under the same conditions are summarized in Figure 5g. As for LIBs, the charging process was initiated first in the SIB systems. During the initial charge process, two different plateaus were observed at ≈3.2–3.8 V for PFC-77, PFC-78, H$_4$L[bipy], and H$_4$TTFTB in SIBs. Similarly, two different plateaus appeared at ≈2.7–3.6 V during the initial discharge process. These behaviors are attributed to the redox activity of the TTF units[21,55,56] and are largely consistent with those observed in the LIB measurements. The electrochemical behavior observed in SIBs, particularly the appearance and disappearance of charge–discharge plateaus, was similar to that in LIBs. The plateau positions closely corresponded to those previously reported for TTF units (charging at 3.4 and 3.6 V; discharging at 2.9 and 3.3 V).[55] Notably, the charge/discharge plateau positions in the first and second cycles were shifted by ≈0.2 V compared to those in

LIBs, which is also consistent with prior studies.[55] This voltage shift is primarily attributed to the difference in the standard electrode potentials between lithium and sodium metals (≈0.331 V vs. standard hydrogen electrode (SHE)), although the observed voltage differences between LIBs and SIBs during cycling may not be entirely explained by this factor alone.[55] Overall, these results confirm that the redox behavior of the TTF units in SIBs is consistent with their established electrochemical characteristics. Additionally, a discharge plateau at ≈1.5–1.9 V was observed during the initial discharge process of H$_4$L[bipy]. By contrast, a gradual charge plateau appeared in the range of 1.7–2.3 V. Similar to the trend observed for TTF units, the charge/discharge plateau positions associated with the bipyridine groups in the first and second cycles were shifted by ≈0.2 V compared to those in LIBs. This shift is likely due to the difference in the standard electrode potentials between lithium and sodium metals (≈0.331 V vs. SHE),[55] supporting the conclusion that this behavior arises from the redox activity of the bipyridine moieties.[56,57] As shown in (Figure S8b, Supporting Information), similar discharge plateaus were also observed in SIBs for the skeletal molecular units containing the 4,4'-bipyridyl bipyridine group. These results are consistent with the bipyridine-derived charge/discharge behavior observed in the hybrid TTF-HOFs examined in this study. Additionally, for the HOF-based materials (PFC-77, PFC-78, and H$_4$L[bipy]), a distinct discharge plateau was observed in the voltage range of 1.0–1.2 V. In contrast, H$_4$TTFTB did not exhibit as clear a plateau in the same potential range as the HOF materials. The low-voltage plateau in the HOF materials tends to become more pronounced after the initial capacity fade, particulary after 100 cycles as shown in Figure S11, Supporting Information, and is presumed to originate from reversible redox reactions of carboxlic groups that are characteristic of hydrogen bonding.[11,68] This behavior suggests that Na$^+$ can reversibly participate in redox reactions while maintaining the hydrogen-bonding network, which is consistent with the mechanism in previous reports.[68] As shown in Figure 5g, the Coulombic efficiency remained consistently at ≈100% over 200 cycles for all tested materials, indicating stable and robust redox behavior, comparable to the performance observed in LIBs.

Table 2 summarizes the maximum discharge capacities within the first five cycles, discharge capacities in the 30th cycle at which the capacity is stabilized following its initial decrease, and discharge capacities after the 200th cycle, and the corresponding capacity retention rates for PFC-77, PFC-78, H$_4$L[bipy], and H$_4$TTFTB in SIBs at a current density of 100 mA g^{-1}. The maximum discharge capacities were achieved during the third, first, first, and first discharge cycles for PFC-77, PFC-78, H$_4$L[bipy], and H$_4$TTFTB, with the corresponding values of 198, 238, 316, and 179 mAh g^{-1}, respectively. At the 30th cycle, for which the capacity is stabilized following its initial decrease, the discharge capacities were 99, 96, 110, and 69 mAh g^{-1}, respectively. In the 30th cycle, the molecular units of PFC-77, PFC-78, H$_4$L[bipy], and H$_4$TTFTB undergo redox processes involving ≈2.53, 2.46, 3.53, and 1.75 electrons, respectively. At the 30th cycle, an average of ≈2.2 electron redox per molecule were observed for PFC-77, PFC-78, and H$_4$TTFTB,
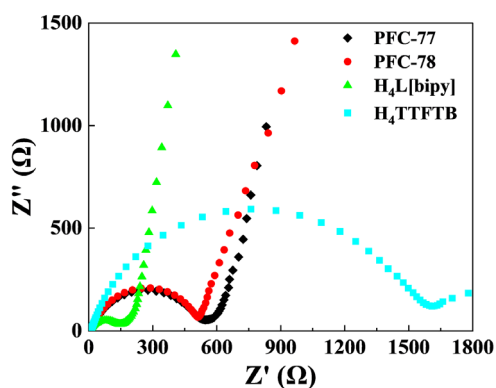

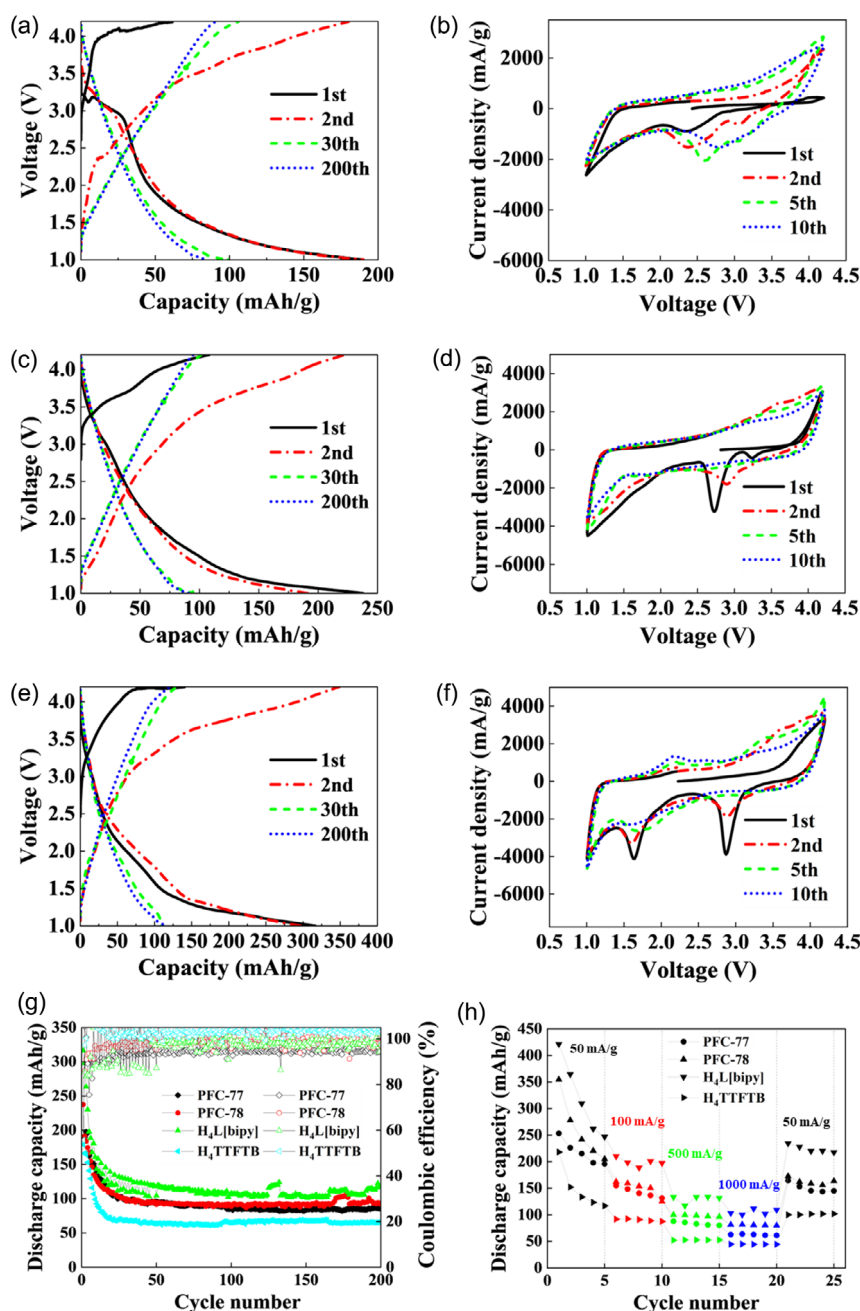**Figure 4.** EIS profiles for H$_4$TTFTB, PFC-77, PFC-78, and H$_4$L[bipy] in LIBs.

Figure 5. a) Discharge/charge curves of PFC-77 at a current density of 100 mA g^{-1} in SIBs. b) CV profiles of PFC-77 in SIBs. c) Discharge/charge curves of PFC-78 at a current density of 100 mA g^{-1} in SIBs. d) CV profiles of PFC-78 in SIBs. e) Discharge/charge curves of H$_4$L[bipy] at a current density of 100 mA g^{-1} in SIBs. f) CV profiles of H$_4$L[bipy] in SIBs. g) Discharge capacity and Coulombic efficiency as a function of cycle number for H$_4$TTFTB, PFC-77, PFC-78, and H$_4$L[bipy] at a current density of 100 mA g^{-1} in SIBs. Filled symbols represent discharge capacity, while unfilled symbols indicate Coulombic efficiency. h) Rate performance of H$_4$TTFTB, PFC-77, PFC-78, and H$_4$L[bipy] in SIBs.

whereas H$_4$L[bipy] exhibited higher redox activity, ≈3.5 electrons per molecule. The redox activity of PFC-77, PFC-78, and H$_4$TTFTB is primarily attributed to the TTF units present in the framework.[21,36,55] By contrast, the higher number of electrons involved in the redox processes of H$_4$L[bipy] which is consistent with their performance in LIBs is likely to be due to the combined redox activity of both the TTF and bipyridine units.[11] The notably high electron transfer numbers observed in SIBs

can be attributed to the redox activity of carboxyl groups[11,68] due to operation over a broader voltage range (1.0–4.2 V) compared to the operation in LIBs. These results underscore the contributions of the redox-active TTF and bipyridine units[11] in SIBs, mirroring their roles in LIBs. Furthermore, the findings suggest that carboxylic groups[11] may play a more significant role in SIBs due to interactions specific to the sodium-ion environment.

Batteries & Supercaps

Research Article
doi.org/10.1002/batt.202500524

Chemistry Europe
European Chemical
Societies Publishing

Table 2. Maximum, 30th cycle, and 200th cycle discharge capacities, along with capacity retention rates after 200 cycles for H_4TTFTB, PFC-77, PFC-78, and $H_4L[bipy]$ at a current density of 100 mA g^{-1} in SIBs. Note that the maximum capacity for PFC-77 occurs at the third cycle, while other values correspond to the first cycle. Discharge capacity retention rates are calculated as the discharge capacity after the 200th cycle divided by the discharge capacity after the 30th cycle after the capacity is stabilized following its initial decrease.

Materials	SIBs			
	Maximum [mAh g^{-1}]	30th cycle [mAh g^{-1}]	200th cycle [mAh g^{-1}]	Retention rates [%]
PFC-77	198	99	85	86
PFC-78	238	96	92	95
$H_4L[bipy]$	316	110	117	107
H_4TTFTB	179	69	66	96

The CV profiles of PFC-77, PFC-78, and $H_4L[bipy]$ in SIBs are shown in Figure 5b,d,f, while that of H_4TTFTB are presented in Figure S9a, Supporting Information. Consistent with the behavior observed in LIBs, for all HOFs and H_4TTFTB in SIBs, two distinct sharp peaks appeared at ≈3.2–3.8 V during the charge process. Conversely, two smaller peaks were observed at ≈2.7–3.6 V during the discharge process. These peaks correspond well with the plateaus observed at 3.2–3.8 and 2.7–3.6 V during the charge and discharge processes shown in Figure 5a,c,e, and S8a, Supporting Information. This indicates that the reversible redox processes of the TTF units occur within the same voltage range as those observed in previous studies (charge: 3.4 and 3.6 V,[55] discharge: 2.9 and 3.3 V[21,36,55]). Similar to the charge–discharge plateaus attributed to the TTF units in SIBs, the CV peak positions were shifted by ≈0.2 V compared to those observed in LIBs. This voltage shift is attributed primarily to the difference between the standard electrode potentials of lithium and sodium metals (≈0.331 V vs. SHE),[55] supporting the occurrence of TTF-derived redox activity in SIB systems. Additionally, a small sharp peak at ≈1.9–2.4 V was observed during the charging process of the hybrid TTF-HOF. By contrast, a gradual discharge peak appeared at ≈1.5–2.3 V. These observations are consistent with the charge–discharge plateaus observed within the same voltage range in Figure 5e. Notably, the charging peaks attributed to the bipyridine units were more pronounced in the SIB systems, whereas such peaks were not clearly observed in the LIB systems. These observations are attributed to the redox processes involving bipyridine groups, further supporting their role in energy storage. Similar to the CV peaks attributed to the TTF units in SIBs, the CV peak positions of the bipyridine units were shifted by ≈0.2 V compared to the previous reports on LIB systems,[55,58] primarily due to the difference between the standard electrode potentials of lithium and sodium metals (≈0.331 V vs. SHE).[55] This voltage shift indicates that bipyridine-derived redox processes also occur in the SIB systems. As shown in Figure S9b, Supporting Information, similar CV peaks were observed for the skeletal molecular units containing the 4,4'-bipyridyl bipyridine group. Specifically, the charge peak appeared in the range of 1.7–2.4 V, while the discharge peak was observed between 1.5

and 2.3 V. Both peaks were more pronounced than those observed in the LIBs. Notably, these peaks closely correspond to the bipyridine-derived charge/discharge features of the hybrid TTF-HOFs in this study, suggesting that the redox activity of the bipyridine moiety is particularly enhanced in SIB systems. Additionally, for all HOFs and H_4TTFTB in SIBs, a small single peak appeared at ≈1.0–1.2 V during the discharge process, with a corresponding charge peak observed at ≈1.2 V. This feature is likely to be due to the redox activity of the carboxylic acid groups,[11,55] because similar CV behavior has been observed in our previous studies on HOFs containing carboxyl functionalities.[50] These findings are also in rough agreement with previous reports on LIB systems.[50,69] However, it is important to consider the differences between LIBs and SIBs, such as the difference between the standard electrode potentials of lithium and sodium metals,[55] when making direct comparisons. Overall, the SIB systems exhibited more pronounced redox activity of carboxylic acid and bipyridine groups than their LIB counterparts, operating over a broader voltage range (1.0–4.2 V). These additional redox contributions may lead to a higher overall capacitance in SIBs compared to LIBs. Similar to the case of LIBs, the CV curves during the first cycle in SIBs showed slight deviations from those observed in the subsequent cycles. This is likely to be due to the changes in the ion intercalation/deintercalation processes, structural rearrangements induced by electrochemical reactions, and the formation of an SEI layer.[66,67] Notably, for almost tested materials, the CV peak intensities in SIBs were larger than those observed in the corresponding LIBs. This difference can be ascribed to the smaller ionic radius of ClO_4^- (2.40 Å)[70] compared to PF_6^- (2.54 Å),[21] which leads to its faster and more quick insertion into and extraction from the cathode framework.[71] As a result, the CV profiles of SIBs tend to exhibit sharper and more well-defined peaks compared to those of LIBs.

The charge–discharge curves, discharge capacity cycling, and Coulombic efficiency, and CV profile of TOKABLACK #5500 at a current density of 50 mA g^{-1} in SIBs are shown in Figure S10b,d,f, Supporting Information. An initial discharge capacity of ≈61.3 mAh g^{-1} was recorded, which decreased over time and stabilized at around 33.7 mAh g^{-1} after 30 cycles. By the 200th cycle, the capacity retained was ≈29.8 mAh g^{-1}. Notably, in the potential windows of 2.7–3.8 (and 1.5–2.4 V), well-defined discharge plateaus appear in the galvanostatic profiles (Figure 5a,c,e and S8a,b, Supporting Information), accompanied by corresponding redox peaks in the CV curves (Figure 5b,d,f and S9a,b, Supporting Information). These electrochemical signatures are absent in control cells using carbon black alone (Figure S10b,f, Supporting Information), indicating that the redox activity arises from the intrinsic properties of the TTF (and bipyridine) units within the HOFs. While a minor portion of the observed capacity may involve capacitive or surface-related contributions from the carbon additive, its overall impact remains limited even at low active material loading, highlighting the dominant role of molecular redox centers in charge storage.

The results for the rate performance of PFC-77, PFC-78, $H_4L[bipy]$, and H_4TTFTB in SIBs are presented in Figure 5h. As expected, the discharge capacities of all HOFs and H_4TTFTB

declined with increasing current densities, most likely due to the limited Na^+ diffusion into the porous structures under high-rate conditions. Nevertheless, all tested materials exhibited superior rate performance in SIBs compared to LIBs, highlighting the potential of TTF-based HOFs as promising cathode materials for SIBs. Similar to the results observed for LIBs, in SIBs all HOFs exhibited higher discharge capacities than H_4TTFTB, even at the elevated current densities. This indicates that the porous architecture of HOFs can facilitate faster charge/discharge processes. As shown in the EIS profiles presented in **Figure 6**, the charge transfer resistances of all HOFs are lower than those of H_4TTFTB in SIBs, suggesting that HOF formation enhances ion conductivity. This improvement is particularly supported by the presence of well-defined pores in the HOF structures, as illustrated in Figure S2a–c, Supporting Information, which likely promote efficient ion transport and reduce charge transfer resistance. However, it is important to note that the charge transfer resistances in SIBs are generally higher than those in LIBs. In the electrolytes used for LIBs and SIBs, the size difference between anions (PF_6^- (2.54 Å) and ClO_4^- (2.40 Å))[21] is relatively small, suggesting that the kinetics of anion insertion/extraction into the active material are likely to be comparable. In contrast, the size difference between cations (Li^+ (0.76 Å) and Na^+ (1.06 Å))[9] is more pronounced, and thus, the influence of cation size on the insertion/extraction process is expected to be more significant. This may account for the higher impedance observed in SIBs, which are driven by the larger Na^+ ions. In addition, the structural and chemical instability of the SEI formed on the Na metal surface may also contribute to the increased impedance. Compared to Li metal, Na metal is more chemically reactive, and the SEI formed on Na is more prone to dissolution in the electrolyte, leading to inferior long-term stability.[72] Furthermore, the SEI on Na metal tends to be compositionally inhomogeneous, resulting in uneven local ionic conductivity and increased interfacial resistance.[73] These problems are exacerbated by the mechanical softness and larger volume changes of Na metal, which cause stress-induced cracking of the SEI during repeated cycling. As a result, the SEI undergoes frequent breakdown and reformation,[73,74] leading to continuous interfacial degradation and disrupted ion transport. This dynamic instability

contrasts with the relatively stable and uniform SEI formation on Li metal surfaces, and thus contributes significantly to the higher impedance of SIBs relative to LIBs.[73,75] Nevertheless, the superior rate performance observed for HOFs in SIBs suggests that the rate-determining steps during the charge/discharge processes may not be the same for SIBs and LIBs.[44] Finally, Table S2–S4, Supporting Information summarize the battery performance characteristics of representative HOFs, TTF-based materials, and bipyridine-based materials reported in previous studies. While direct comparison is limited by the differences in the experimental conditions, such as the current densities, voltage windows, and battery configurations, these data provide useful context for evaluating the relative performance of our materials.

2.3. Role of Hybrid TTF-HOF Architecture in Enhancing Electrochemical Performance

The high initial discharge capacities observed for all HOFs are primarily attributed to electrolyte decomposition and the formation of an SEI layer.[66,67] While LIBs and SIBs often operate via similar electrochemical mechanisms due to the chemical similarities of Li^+ and Na^+ ions,[76] comparison of LIB and SIB performance characteristics shows that both the discharge capacities and capacity retention rates were consistently higher and more stable in SIBs across all tested samples. As shown in Table 1, the discharge capacities of PFC-77, PFC-78, $H_4L[bipy]$, and H_4TTFTB decreased gradually to 39, 44, 45, and 31 mAh g^{-1}, respectively, after 200 cycles in LIBs. The corresponding retention rates, defined as the ratio of capacity at the 200th cycle to that at the 30th cycle, were 77, 62, 73, and 74%, respectively. By contrast, in SIBs, the discharge capacities of the same materials decreased to 85, 92, 117, and 66 mAh g^{-1}, with significantly higher retention rates of 86, 95, 107, and 96%, respectively, as shown in Table 2. These differences can be caused by inherent variations in the thermodynamic and kinetic behaviors of the two systems.[77] In this study, they can particularly be attributed in part to the broader voltage window used during electrochemical testing (1.0–4.2 V for SIBs vs. 1.5–4.2 V for LIBs), allowing access to additional redox processes. Moreover, in the HOF materials, carboxylic groups in SIBs showed more reversible redox behavior, as evidenced by a distinct discharge peak at 1.0–1.2 V,[68] in contrast to the more irreversible reactions observed in LIBs.[59] These combined factors contribute to the enhanced electrochemical performance observed in SIB systems.

The discharge capacities of all HOFs were greater than those of H_4TTFTB after both the 30th and 200th cycles in both LIBs and SIBs, indicating that the formation of extended HOF architectures enhances resistance to dissolution in electrolytes. This conclusion is supported not only by the higher long-term capacities but also by the results of the solubility tests (Figure S12–S14, Supporting Information) which revealed that TTF-HOFs exhibit significantly lower solubility in both 1.0 M $LiPF_6$ in EC/DEC and 1.0 M $NaClO_4$ in EC/PC than H_4TTFTB, and 4,4′-bipyridyl. Ultraviolet visible (UV–vis) spectroscopy-based solubility tests with electrodes immersed in 1.0 M $LiPF_6$ in EC/DEC (1:1 v/v) and 1.0 M $NaClO_4$
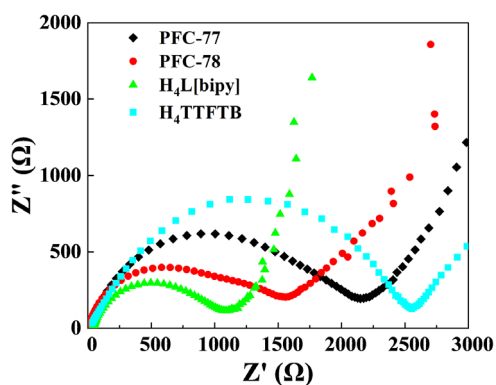

Figure 6. EIS profiles for H_4TTFTB, PFC-77, PFC-78, and $H_4L[bipy]$ in SIBs.

Batteries & Supercaps

Research Article
doi.org/10.1002/batt.202500524

Chemistry Europe
European Chemical
Societies Publishing

in EC/PC (1:1 v/v) were also conducted using UV–vis spectroscopy as shown in Figure S14 and S15, Supporting Information. According to previous reports,[42,78,79] absorbance in the 200–300 nm range is considered indicative of organic species dissolution. In our study, a clear peak was observed around 200–300 nm in all samples. This is attributed to π–π^* transitions of the aromatic and conjugated structures,[78] such as the TTF unit and aromatic carboxylic acids, which are present in both the molecular precursor and the HOF-based frameworks. For the molecular precursor H_4TTFTB, the absorbance at $\approx$230 nm was $\approx$0.24 and $\approx$0.11 after 1 day, increasing slightly to $\approx$0.28 and $\approx$0.12 after 7 days in LIBs and SIBs, respectively, indicating significant dissolution from an early stage. In contrast, for the HOF-based electrodes (PFC-77, PFC-78, and H_4L[bipy]), the absorbance remained significantly lower, below $\approx$0.09 and $\approx$0.07 after 1 day, and below $\approx$0.14 and $\approx$0.08 after 7 days in LIBs and SIBs, respectively, suggesting much more limited dissolution compared to the molecular precursor. These results imply that formation of the HOF structure effectively suppresses solubility in the electrolyte. In addition, these results revealed that both the HOF-based and molecular precursor (H_4TTFTB) electrodes exhibited more reduced dissolution in SIBs, further supporting the enhanced electrochemical performance observed in SIB systems. Although some dissolution may still occur during battery operation, this could be attributed to the higher solubility of redox-active species generated during cycling compared to the neutral active materials. Nevertheless, the observed solubility suppression in the as-prepared electrode samples highlights a key advantage of HOF formation: enhanced resistance to electrolyte-mediated decomposition, particularly in comparison to discrete organic molecules.

Among the tested materials, hybrid TTF-HOFs incorporating bipyridine units exhibited superior discharge capacities after both the 30th and 200th cycles in both LIBs and SIBs, with the enhancement particularly pronounced in SIBs. This improvement is most likely due to the synergistic redox activity of the TTF and bipyridine units. In SIBs, the greater capacity may be further attributed to the broader voltage window (1.0–4.2 V) and the additional redox activity of carboxylate groups. The superior dissolution resistance of hybrid TTF-HOFs is also supported by their lower solubility compared to TTF-HOFs without bipyridine units, as shown in Figure S12 and S13, Supporting Information. The incorporation of nitrogen-containing heterocycles (bipyridine units) is believed to strengthen the framework and further suppress solubility in the electrolytes.[54] Additionally, hybrid TTF-HOFs showed higher maximum capacities in the initial cycles compared to the HOFs that lack redox-active units,[44] even though the issue of gradual capacity fading is not eliminated. This enhancement is attributed to the presence of inherently stable, redox-active TTF and bipyridine moieties. These results underscore the importance of designing HOFs with synergistic redox-active components as a promising strategy to boost electrochemical performance in both LIBs and SIBs.

In both LIBs and SIBs, TTF-HOFs demonstrated superior battery capacities compared to H_4TTFTB, even at high current densities as shown in Figure 3h and 5h. This improvement is primarily attributed to the porous architecture of the HOFs, which facilitates more efficient ion transport during the charge and discharge cycles. EIS measurements further support this interpretation, indicating that the charge–transfer resistance of H_4TTFTB is higher than that of TTF-HOFs, as shown in Figure 4 and 6. Notably, the hybrid TTF-HOFs incorporating bipyridine units exhibited even greater battery capacities at high current densities in both LIBs and SIBs compared to the TTF-HOFs without bipyridine units. EIS analysis revealed that the hybrid TTF-HOFs also possess lower ionic conductivity than the TTF-HOFs without bipyridine units. This conclusion is further corroborated by the results of the nitrogen gas adsorption/desorption measurements presented in Figure S7a–c, Supporting Information, which show that the hybrid TTF-HOFs have larger pore sizes than bipyridine-free TTF-HOFs, thereby facilitating faster ion (de)insertion during the charge and discharge processes. These observations collectively suggest that the porous framework, the synergistic redox activity units, and the incorporation of robust nitrogen-containing units in HOFs play essential roles in improving their electrochemical performance relative to that of their molecular counterparts.

2.4. Redox Mechanism and Ion Insertion/Deinsertion Behavior during Charge and Discharge Processes

As shown in Figure 2a,c, the redox processes of the TTF and bipyridine units follow a P-type mechanism,[17–22,53] wherein these moieties undergo reversible oxidation during charging by losing electrons and forming positively charged species. These charges are compensated by the insertion of counter anions, such as PF_6^-, from the electrolyte.[21] To investigate the involvement of anion insertion and extraction during electrochemical cycling, we performed SEM with energy dispersive X-ray (SEM–EDX) spectroscopy to estimate the changes in the elemental composition of the electrodes in their pristine, charged, and discharged states. Figure S16–S18, Supporting Information show the elemental maps of sulfur (S), phosphorus (P), and fluorine (F) for the PFC-78, H_4L[bipy], and H_4TTFTB cathodes in LIBs, respectively. The S signal originates from the TTF units, while the P and F signals originate from the PF_6^- electrolyte salt. As illustrated in Figure S19a–c, Supporting Information, for all tested cathodes, the F/S and P/S weight ratios increased after charging and decreased after discharging. This repeated trend confirms the reversible insertion and extraction of PF_6^- anions into and from the HOF structures during the electrochemical cycling. By contrast, as shown in Figure S19c, Supporting Information, the precursor (H_4TTFTB) exhibited irreversible behavior distinct from that of PFC-78 and H_4L[bipy]. This may be attributed to the higher solubility of the precursor compared to the HOFs, which likely hinders the effective function of the redox-active S sites. As a result, the redox process becomes irreversible, leading to nonreversible trends in the F/S and P/S weight ratios during the charge–discharge cycles. Unlike metal cations, PF_6^- anions are relatively bulky, leading to a more delocalized charge distribution and weaker interactions with solvent molecules. Consequently, PF_6^- anions are less solvated and can diffuse more rapidly

Batteries & Supercaps

Research Article
doi.org/10.1002/batt.202500524

Chemistry
Europe
European Chemical
Societies Publishing

through the electrolyte and into the electrode materials.[21] This anion-driven P-type redox mechanism, in combination with the highly porous architecture of the HOFs that promotes efficient ion transport and low charge–transfer resistance, contributes significantly to the enhanced rate performance observed in Figure 3h and 5h. The concerted effect of these features enables faster charge/discharge kinetics and underscores the potential of HOF-based materials for high-power rechargeable battery applications.

Figure S20a–c, Supporting Information show the ex situ PXRD profiles of PFC-78, H_4L[bipy], and H_4TTFTB cathodes during the charge and discharge processes in both LIBs and SIBs. In LIBs, the PXRD patterns reveal structural differences between the pristine powders and the electrode states, indicating minor rearrangements of the structures that are likely due to the use of anhydrous *N*-methylpyrrolidone (NMP) during the preparation of the electrode slurry. After the charge process, the oxidation of TTF (and bipyridine) units resulted in decreased peak intensities across all samples, suggesting partial amorphization due to the insertion of the PF_6^- anions from the electrolyte. During the discharge process, the extraction of PF_6^- led to increased peak intensities, indicating a partial recovery of crystallinity.[33] This reversible ion intercalation process involving repeated structural ordering and disordering is believed to contribute to the gradual capacity fading observed after multiple charge/discharge cycles, which is reflected in the slower redox reactions and the eventual disappearance of the plateaus as shown in Figure 3a,c,e, and S8a, Supporting Information. Similar trends were observed for SIBs. The charge process induced the oxidation of the redox-active units, accompanied by reduced PXRD peak intensities due to the ClO_4^- anion insertion into the frameworks, leading to partial amorphization. During the discharge process, ClO_4^- anions were extracted, restoring peak intensities and suggesting enhanced crystallinity.[33] This cyclic crystallinity change which is driven by repeated ion insertion and extraction also contributes to capacity fading and the progressive disappearance of voltage plateaus over long-term cycling, as observed in Figure 5a,c,e, and S8a, Supporting Information. This effect was particularly pronounced in TTF-based HOFs used in SIBs. Moreover, SEM images of the pristine cathodes, and the cathodes after charging and discharging were obtained for PFC-78, H_4L[bipy], and H_4TTFTB in both LIBs and SIBs. As shown in Figure S21–S23, Supporting Information, no significant changes in either particle size or morphology were observed, even after cycling. These SEM results suggest that the particle integrity of our tested materials is largely preserved during the electrochemical reactions, indicating good structural stability under operating conditions. Meanwhile, as shown in Figure S16c, Supporting Information, the precursor (H_4TTFTB) exhibited behavior distinct from those of PFC-78 and H_4L[bipy]. This difference may be attributed to the lower crystallinity of the vacancy-free precursor compared to the HOFs, where the presence of vacancies likely facilitates anion insertion and deinsertion.

The porous architecture of HOFs plays a key role in facilitating the intercalation and deintercalation of Li^+ and Na^+ ions. These results underscore the promise of HOF materials as active electrode components for both LIBs and SIBs. However, capacity fading caused by the dissolution of active materials remains a significant challenge. For practical applications, long-term capacity retention will require strategies to prevent structural degradation under electrochemical stress, potentially through targeted chemical modifications to suppress HOF dissolution in electrolytes.[80] Additionally, it is essential to improve current-collecting ability within the electrode by using conductive additives,[34] as well as developing lightweight materials with abundant redox sites to achieve higher capacity.[33]

3. Conclusion

In this study, we evaluated TTF-based HOFs as cathode active materials for rechargeable LIBs and SIBs. These materials, featuring both redox-active centers and porous frameworks, exhibited promising electrochemical performance while maintaining structural integrity during charge/discharge cycling even after HOF formation. In particular, hybrid TTF-HOFs incorporating bipyridine units demonstrated superior capacities owing to the synergistic redox activity and enhanced structural robustness provided by nitrogen-containing heterocycles. These superior performance characteristics were particularly pronounced in SIB systems, owing to the more pronounced redox activity of carboxylic acid and bipyridine groups over a broader operating voltage range (1.0–4.2 V) compared to that of LIBs. Our findings underscore the advantages of the integration of synergistic redox-active units within extended HOF architectures which offer improved ion transport and reduced solubility in electrolytes and enhanced battery capacities after cycling compared to their molecular analogs. CV experiments further confirmed distinct redox activity due to the TTF moieties ($\approx$3.4–4.0/3.0–3.6 V in LIBs and 3.2–3.8/2.7–3.6 V in SIBs) and bipyridine units (approximately no evident activity/2.0–2.5 V in LIBs and 1.9–2.4/1.5–2.3 V in SIBs) during the charge and discharge processes, contributing to multistep charge storage mechanisms.

Despite these promising results, some challenges remain, most notably the initial capacity decay and gradual capacity fading during extended cycling that are likely due to the partial HOF dissolution and structural degradation under electrochemical conditions. Addressing these limitations will require the development of more robust HOF frameworks through molecular design strategies that reinforce hydrogen bonding and backbone stability, as well as the optimization of the electrolyte compositions to suppress solubility. Future work should also include theoretical studies (e.g., density functional theory (DFT) calculations) to elucidate electronic structures, redox potentials, and ion transport pathways, alongside advanced synchrotron radiation spectroscopic techniques such as X-ray absorption spectroscopy to track structural changes in operando. Collectively, these insights provide a foundation for rational design of next-generation HOF-based electrode materials and highlight the potential of incorporating porous frameworks, synergistic redox-active units, and heterocyclic frameworks in sustainable energy storage technologies.

4. Experimental Section

Material Preparation: Synthesis of 2,3,6,7-tetra(4-Ethoxycarbonylphenyl)Tetrathiafulvalene (Et$_4$TTFTB)

Et$_4$TTFTB, a precursor for H$_4$TTFTB, was synthesized using a modified procedure based on a previously reported method.[81] In a 100 mL three-neck round-bottom flask equipped with a nitrogen atmosphere, palladium (II) acetate (Pd(OAc)$_2$) (83.9 mg, 0.37 mmol, Tokyo Chemical Industry (TCI)), tri-tert-butylphosphonium tetrafluoroborate (P(But)$_3$·HBF$_4$) (325.9 mg, 1.12 mmol, TCI), and cesium carbonate (Cs$_2$CO$_3$) (2444.0 mg, 7.50 mmol, Wako) were dissolved in tetrahydrofuran (THF, 15 mL). The reaction mixture was stirred and heated at reflux at 70 °C for 10 min. Subsequently, a solution of TTF (307.6 mg, 1.51 mmol, TCI) and ethyl 4-bromobenzoate (1718.0 mg, 7.5 mmol, TCI) in THF (15 mL) was added to the reaction mixture. The resulting mixture was further heated at reflux at 70 °C for 20 h under continuous stirring. Upon completion of the reaction, the mixture was cooled to room temperature (≈25 °C) and extracted three times with chloroform. The combined organic layers were washed with brine, dried over anhydrous sodium sulfate (Na$_2$SO$_4$), and concentrated under reduced pressure. The crude product was purified via column chromatography on silica gel using dichloromethane as the eluent, and concentrated under reduced pressure to give Et$_4$TTFTB as a red solid.

Material Preparation: Synthesis of Tetrathiafulvalene-Tetrabenzoate (Tetrathiafulvalene Tetrabenzoic Acid · 1.5 CH$_3$OH, H$_4$TTFTB)

H$_4$TTFTB, a precursor for TTF-HOFs (PFC-77 and PFC-78) and TTF-hybrid-HOFs (H$_4$L[bipy]), was synthesized using a modified procedure based on a previously reported method.[82] Methanol, THF, and purified water were degassed by bubbling nitrogen gas for 10 min prior to use. Et$_4$TTFTB (1211 mg, 2.15 mmol) was suspended in a degassed mixture of methanol (20 mL) and THF (20 mL) in a 100 mL round-bottom flask. Subsequently, a solution of potassium hydroxide (1074.2 mg, 19.14 mmol, Wako) in degassed purified water (20 mL) was added dropwise to the suspension under nitrogen atmosphere. The reaction mixture was heated at reflux at 70 °C and stirred continuously for 20 h. After completion, the reaction mixture was cooled to room temperature (≈25 °C), and the volatile components were removed under reduced pressure using a rotary evaporator. To the resulting residue, 1 M HCl (10 mL) was added, leading to the formation of a maroon precipitate. The precipitate was collected by suction filtration, washed thoroughly with water (50 mL), and dried under high vacuum for 12 h. The final product, H$_4$TTFTB, was obtained as a dark brown solid.

Material Preparation: Synthesis of TTF-HOFs: PFC-77 and PFC-78

TTF-HOFs: PFC-77 and PFC-78 were synthesized using a previously reported method with modifications.[52]

PFC-77: H$_4$TTFTB (93.3 mg, 0.14 mmol) was dissolved in THF (30 mL) in a vial. The solution was stirred at room temperature (≈25 °C) for 10 min, and then allowed to evaporate spontaneously over 3 days at ambient conditions. After completion, PFC-77 was collected as a dark brown solid at the bottom of the vial.

PFC-78: H$_4$TTFTB (90.0 mg, 0.13 mmol) was dissolved in acetone (20 mL) in a 100 mL round-bottom flask under nitrogen atmosphere.

The solution was stirred and heated at reflux at 55 °C for 2 h. After completion, the solution was filtered to remove any undissolved impurities. The resulting filtrate was transferred to a vial and allowed to evaporate spontaneously at ambient conditions over 5 days. PFC-78 was collected as a dark brown solid at the bottom of the vial.

Material Preparation: Synthesis of TTF-Hybrid-HOFs: H$_4$L[bipy]

TTF-hybrid-HOFs: H$_4$L[bipy] were synthesized by modifying a previously reported method.[19]

H$_4$L[bipy]: H$_4$TTFTB (97.9 mg, 0.14 mmol) and 4,4'-bipyridyl (47.6 mg, 0.30 mmol, Wako) was dissolved in THF (10 mL) in a 100 mL round-bottom flask under nitrogen atmosphere. The solution was stirred and heated at reflux at 55 °C for 2 h. After completion, the solution was filtered to remove any undissolved impurities. The resulting filtrate was transferred to a vial and allowed to evaporate spontaneously at ambient conditions over 3 days. H$_4$L[bipy] was collected as a dark brown solid at the bottom of the vial.

Measurements: PXRD Analysis

PXRD measurements were conducted using a MiniFlex 600 diffractometer (Rigaku) with Cu Kα_1 radiation (wavelength $\lambda = 1.5405$ Å). The data were collected over a 2θ range of 2°–30° at a scan speed of 20° min^{-1}. The operating voltage and current were set to 40 kV and 15 mA, respectively. These measurements were performed at room temperature (≈25 °C).

Measurements: FTIR

FTIR spectra were recorded using an IRAffinity-1S spectrometer (SHIMADZU) over a wavenumber range between 599.8618 and 4000.364 cm^{-1}. These measurements were performed at room temperature (≈25 °C).

Measurements: SEM–EDX

SEM–EDX was performed on a FlexSEM 1000 (HITACHI) system, where the voltage was set 5 kV with secondary electrons for SEM observation and 15 kV with backscattered electrons for EDX analysis. The samples were placed on the carbon tapes, and then, SEM images of the samples were obtained under high-vacuum conditions. The magnification was set at 100 times.

Measurements: N$_2$ Gas Adsorption and Desorption Measurements

N$_2$ gas adsorption/desorption measurements were performed at 77 K using a Belsorp-max surface area and pore size analyzer (BEL Japan, Inc.). Before measurements, the HOF samples were activated under a vacuum at 60 °C for 12 h in the case of PFC-77 and PFC-78 or for 30 min in the case of H$_4$L[bipy]. Data analysis was conducted with the BELMaster software, using the Brunauer–Emmett–Teller method and nonlocal DFT.

Measurements: Dissolution Tests

Dissolution tests were conducted using both powder and electrode samples. For the powder-based tests, 0.002 g of the sample was

Batteries & Supercaps

Research Article
doi.org/10.1002/batt.202500524

Chemistry Europe
European Chemical
Societies Publishing

dispersed in 2 mL of electrolyte (either 1.0 M $LiPF_6$ in EC/DEC (1:1 v/v) or 1.0 M $NaClO_4$ in EC/PC (1:1 v/v)) in a glass vial, followed by sonication for 30 s and storage at room temperature ($\approx$25 °C) for 1 day. For the electrode-based tests, each electrode was cut into four equal pieces, and each piece was immersed in 2 mL of the electrolyte in a glass vial. These samples were then stored at room temperature ($\approx$25 °C) for 1 or 7 days prior to analysis.

Measurements: UV–Vis Absorption Spectroscopy

UV–vis spectra were recorded using a UV-3600 Plus UV–vIS–NIR spectrophotometer (SHIMADZU) with a 1 cm path length quartz cuvette. The data were collected over a wavelength range of 150–1,000 nm at room temperature ($\approx$25 °C). After the specified soaking period of the electrode samples in the dissolution tests, 0.2 mL of the solution in which the electrode had been immersed was transferred to a quartz cuvette, and 3.0 mL of the corresponding fresh electrolyte was subsequently added to the cuvette prior to measurement. The cuvette was rinsed three times with ethanol between sample measurements, and the next sample was introduced without drying. Deionized water was used as a blank to correct for background absorption and the corresponding fresh electrolyte was used as a reference. In all cases, a prominent absorption peak was observed at around 200–300 nm, which is consistent with previously reported absorption features.[42,78,79]

Measurements: Battery Fabrication

Cathodes were prepared using the following procedure. First, H_4TTFTB; TTF-HOFs (PFC-77, PFC-78); or TTF-hybrid-HOFs (H_4L[bipy]), and TOKABLACK #5500 (Tokai Carbon) as a conductive carbon were ground in an agate mortar with a pestle for 40 min. A carboxymethyl cellulose sodium salt (CMC) binder (Wako) was then added, and the mixture was further ground for 40 min. The weight ratio of H_4TTFTB; TTF-HOFs (PFC-77, PFC-78); or TTF-hybrid-HOFs (H_4L[bipy]), TOKABLACK #5500, and CMC was set to 30:60:10 to enhance electronic conductivity. The weight ratio of TOKABLACK #5500 to CMC was 90:10 were performed to evaluate the effect of conductive carbon on the battery performance, where the charging process was initiated first and observations were recorded.

Next, a slurry was prepared by adding anhydrous N-methylpyrrolidone (NMP) (Sigma-Aldrich) to the ground mixture. The slurry was applied to aluminum foil (thickness: 20 μm) using the doctor blade method and dried overnight under vacuum. The coated foil was then cut into disks (diameter: $\varphi = 15.95$ mm) to serve as the active electrode material. CR2032 coin-type cells were assembled in an argon-filled glovebox. The prepared cathode materials were used as the positive electrode, and lithium foil (thickness: 0.2 mm, φ: 15.50 mm) or sodium foil (φ: 15.50 mm) served as the anode. For LIBs, a polypropylene separator (CS Tech, φ: 17.00 mm) was used, while for SIBs, a glass microfiber separator (Whatman, grade GF/D, φ: 17.00 mm) was used to prevent active material dissolution. The electrolyte for LIBs was 1.0 M $LiPF_6$ in EC/DEC (1:1 v/v) (Kishida Chemical), while for SIBs, it was 1.0 M $NaClO_4$ in EC/PC (1:1 v/v) (Tomiyama Pure Chemical Industries, Ltd.), both selected to minimize undesirable side reactions. The fabricated CR2032 coin-type cells were utilized for galvanostatic charge–discharge testing, CV measurements, and (EIS analysis.

Measurements: Galvanostatic Charge/Discharge Tests

Galvanostatic charge/discharge tests were performed using an HJ1020mSD8 system (HOKUTO DENKO) at room temperature ($\approx$25 °C), starting with the charging process. As-prepared CR2032 coin-type cells, without prior charge/discharge cycling, were cycled at a current density of 100 mA g^{-1} within the voltage ranges of 1.5–4.2 V (vs. Li^+/Li) for LIBs and 1.0–4.2 V (vs. Na^+/Na) for SIBs.

Measurements: CV Measurements

CV measurements were carried out using an HZ-Pro S12 system (HOKUTO DENKO) over the voltage ranges of 1.5–4.2 V (vs. Li^+/Li) and 1.0–4.2 V (vs. Na^+/Na) at a scan rate of 10 mV s^{-1} at room temperature ($\approx$25 °C). As-prepared CR2032 coin-type cells, without prior charge/discharge cycling, were used for both LIBs and SIBs.

Measurements: Rate Performance Analysis

Rate performance was evaluated using an HJ1020mSD8 7system (HOKUTO DENKO) at room temperature ($\approx$25 °C), starting with the charge process. As-prepared CR2032 coin-type cells, without prior charge/discharge cycling, were cycled at the current densities of 50, 100, 500, and 1,000 mA g^{-1}. Each current density was applied for five cycles, resulting in a total of 25 cycles. Voltage ranges of 1.5–4.2 V (vs. Li^+/Li) and 1.0–4.2 V (vs. Na^+/Na) were employed.

Measurements: EIS Analysis

EIS measurements were conducted on an HZ-Pro S12 system (HOKUTO DENKO) across a frequency range from 100 kHz to 10 mHz at room temperature ($\approx$25 °C). As-prepared CR2032 coin-type cells, without prior charge/discharge cycling, were used for both LIBs and SIBs.

Supporting Information

The data supporting this article have been included as the Supporting Information (SI): schematic diagrams of precursors and TTF-based HOFs; powder characterization results including PXRD, FT-IR spectroscopy, SEM images, and nitrogen gas adsorption/desorption measurements; additional discharge/charge curves and CV profiles; solubility tests; UV-Vis spectroscopy; EDX mappings after cycling; F/S and P/S atomic ratio after cycling; ex-situ PXRD after cycling; SEM images after cycling; and performance metrics of representative samples as cathode materials in this study and previous reports. The authors have also cited additional references within the SI.

Acknowledgements

Conflict of Interest

The authors declare no conflict of interest.

Data Availability Statement

Research data are not shared.

[1] A. Kanwade, S. Gupta, A. Kankane, M. K. Tiwari, A. Srivastava, A. K. S. Jena, S. C. Yadav, P. M. Shirage, *RSC Adv.* **2022**, *12*, 23284.
[2] J. Ren, H. Zhu, Y. Fang, W. Li, S. Lan, S. Wei, Z. Yin, Y. Tang, Y. Ren, Q. Liu, *Carbon Neutralization* **2023**, *2*, 339.
[3] S. Li, Y. Sun, Y. Pang, S. Xia, T. Chen, H. Sun, S. Zheng, T. Yuan, *Asia-Pac J. Chem. Eng.* **2022**, *17*, e2762.
[4] N. Yabuuchi, K. Kubota, M. Dahbi, S. Komaba, *Chem. Rev.* **2014**, *114*, 11636.
[5] S. Lee, A. Manthiram, *ACS Energy Lett.* **2022**, *7*, 3058.
[6] B. Dunn, H. Kamath, J.-M. Tarascon, *Science* **2011**, *334*, 928.
[7] W. Fu, Y. Wang, K. Kong, D. Kim, F. Wang, G. Yushin, *Nanoenergy Adv.* **2023**, *3*, 138.
[8] L. Liang, W.-H. Lai, Z. Miao, S.-L. Chou, *Small* **2018**, *14*, 1702514.
[9] M.-D. Slater, D. Kim, E. Lee, C.-S. Johnson, *Adv. Funct. Mater.* **2013**, *23*, 947.
[10] K. Diederichsen, E. McShane, B.-D. McCloskey, *ACS Energy Lett.* **2017**, *2*, 2563.
[11] J. Heiska, M. Nisula, M. Karppinen, *J. Mater. Chem. A* **2019**, *7*, 18735.
[12] H. Lyu, X.-G. Sun, S. Dai, *Adv. Energy Sustainability Res.* **2021**, *2*, 2000044.
[13] Z. Song, Y. Qian, T. Zhang, M. Otani, H. Zhou, *Adv. Sci.* **2015**, *2*, 1500124.
[14] M.-C. Díaz, B.-M. Illescas, C. Seoane, N. Martín, *J. Org. Chem.* **2004**, *69*, 4492.
[15] Y.-G. Weng, W.-Y. Yin, M. Jiang, J.-L. Hou, J. Shao, Q.-Y. Zhu, J. Dai, *ACS Appl. Mater. Interfaces* **2020**, *12*, 52615.
[16] J.-O. Jeppesen, M.-B. Nielsen, J. Becher, *Chem. Rev.* **2004**, *104*, 5115.
[17] D. Lorcy, N. Bellec, M. Fourmigué, N. Avarvari, *Coord. Chem. Rev.* **2009**, *253*, 1398.
[18] M. Bøndsted Nielsen, C. Lomholta, J. Becher, *Chem. Soc. Rev.* **2000**, *29*, 153.
[19] X. Zheng, N. Xiao, Z. Long, L. Wang, F. Ye, J. Fang, L. Shen, X. Xiao, *Synth. Met.* **2020**, *263*, 116365.
[20] N. Daub, K. H. Hendriks, R. A. J. Janssen, *Batteries Supercaps* **2022**, *5*, e202200386.
[21] H. Kye, Y. Kang, D. Jang, J. Kwon, B.-G. Kim, *Adv. Energy Sustainability Res.* **2022**, *3*, 2200030.
[22] G. Valente, R. Dantas, P. Ferreira, R. Grieco, N. Patil, A. Guillem-Navajas, D. R.íguez-S. Miguel, F. Zamora, R. Guntermann, T. Bein, J. Rocha, M. H. Braga, K. Strutyński, M. Melle-Franco, R. Marcilla, M. Souto, *J. Mater. Chem. A* **2024**, *12*, 24156.
[23] L. S. Xie, S. S. Park, M. J. Chmielewski, H. Liu, R. A. Kharod, L. Yang, M. G. Campbell, M. Dincă, *Angew. Chem. Int. Ed.* **2020**, *59*, 19623.
[24] L. S. Xie, G. Skorupskii, M. Dincă, *Chem. Rev.* **2020**, *120*, 8536.
[25] H.-Y. Wang, J.-Y. Ge, C. Hua, C.-Q. Jiao, Y. Wu, C. F. Leong, D. M. D'Alessandro, T. Liu, J.-L. Zuo, *Angew. Chem. Int. Ed.* **2017**, *56*, 5465.
[26] J. Castells-Gil, S. Mañas-Valero, I. J. Vitórica-Yrezábal, D. Ananias, J. Rocha, R. Santiago, S. T. Bromley, J. J. Baldoví, E. Coronado, M. Souto, G. M. Espallargas, *Chem. Eur. J.* **2019**, *25*, 12636.
[27] J. Su, T.-H. Hu, R. Murase, H.-Y. Wang, D. M. D'Alessandro, M. Kurmoo, J.-L. Zuo, *Inorg. Chem.* **2019**, *58*, 3698.
[28] J. Su, S. Yuan, T. Wang, C. T. Lollar, J.-L. Zuo, J. Zhang, H.-C. Zhou, *Chem. Sci.* **2020**, *11*, 1918.
[29] M. Souto, A. Santiago-Portillo, M. Palomino, I. J. Vitórica-Yrezábal, B. J. C. Vieira, J. C. Waerenborgh, S. Valencia, S. Navalón, F. Rey, H. García, G. Mínguez Espallargas, *Chem. Sci.* **2018**, *9*, 2413.
[30] Y. Zhou, F. Yu, J. Su, M. Kurmoo, J.-L. Zuo, *Angew. Chem. Int. Ed.* **2020**, *59*, 18763.
[31] M. Jiang, Y.-G. Weng, Z.-Y. Zhou, C.-Y. Ge, Q.-Y. Zhu, J. Dai, *Inorg. Chem.* **2020**, *59*, 10727.
[32] M. Kato, K. Senoo, M. Yao, Y. Misaki, *J. Mater. Chem. A* **2014**, *2*, 6747.
[33] W. Yan, J. Su, Z.-M. Yang, S. Lv, Z. Jin, J.-L. Zuo, *Small* **2021**, *17*, 2005209.
[34] Y. Misaki, S. Noda, M. Kato, T. Yamauchi, T. Oshima, A. Yoshimura, T. Shirahata, M. Yao, *ChemSusChem* **2020**, *13*, 2312.
[35] Q. Pan, S. Chen, C. Wu, Z. Zhang, Z. Li, Y. Zhao, *ACS Appl. Mater. Interfaces* **2019**, *11*, 46070.
[36] Y. Inatomi, N. Hojo, T. Yamamoto, S. Watanabe, Y. Misaki, *ChemPlusChem* **2012**, *77*, 973.
[37] A. Yoshimura, K. Hemmi, H. Moriwaki, R. Sakakibara, H. Kimura, Y. Aso, N. Kinoshita, R. Suizu, T. Shirahata, M. Yao, H. Yorimitsu, K. Awaga, Y. Misaki, *ACS Appl. Mater. Interfaces* **2022**, *14*, 35978.
[38] A.-G. Slater, A.-I. Cooper, *Science* **2015**, *348*, aaa8075.
[39] Z. Wang, H. Tao, Y. Yue, *ChemElectroChem* **2019**, *6*, 5358.
[40] R. Du, Y. Wu, Y. Yang, T. Zhai, T. Zhou, Q. Shang, L. Zhu, C. Shang, Z. Guo, *Adv. Energy Mater.* **2021**, *11*, 2100154.
[41] W. Yan, J. Su, Z.-M. Yang, S. Lv, Z. Jin, J.-L. Zuo, *Small Struct.* **2022**, *3*, 2200126.
[42] Y. Luo, K. Jia, X. Li, J. Zhang, G. Huang, C. Zhong, L. Zhu, F. Wu, *ChemSusChem* **2024**, *17*, e202301847.
[43] Z.-M. Yang, Y. Wang, M.-H. Zhang, Z.-Y. Hou, S.-P. Zhao, X. Han, S. Yuan, J. Su, Z. Jin, J.-L. Zuo, *Energy Storage Mater.* **2025**, *75*, 104038.
[44] K. Wakamatsu, S. Furuno, Y. Yamaguchi, R. Matsushima, T. Shimizu, N. Tanifuji, H. Yoshikawa, *ACS Appl. Energy Mater.* **2023**, *6*, 9124.
[45] C. Chen, L. Shen, H. Lin, D. Zhao, B. Li, B. Chen, *Chem. Soc. Rev.* **2024**, *53*, 2738.
[46] X. Liu, X. Yang, H. Wang, I. Hisaki, K. Wanga, J. Jiang, *J. Mater. Chem. A* **2022**, *10*, 1808.
[47] C. Guo, B. Han, W. Sun, Y. Cao, Y. Zhang, Y. Wang, *Angew. Chem. Int. Ed.* **2022**, *61*, e202213276.
[48] Y.-L. Wu, N. E. Horwitz, K.-S. Chen, D. A. Gomez-Gualdron, N. S. Luu, L. Ma, T. -C. Wang, M. C. Hersam, J. T. Hupp, O. K. Farha, R. Q. Snurr, M. R. Wasielewski, *Nat. Chem.* **2017**, *9*, 466.
[49] Y. Wu, X. Mao, M. Zhang, X. Zhao, R. Xue, S. Di, W. Huang, L. Wang, Y. Li, Y. Li, *Adv. Mater.* **2021**, *33*, 2106079.
[50] K. Wakamatsu, Y. Yamaguchi, S. Furuno, H. Wang, H. Yoshikawa, *ChemElectroChem* **2024**, *11*, e202300607.
[51] K. Wakamatsu, Y. Yamaguchi, S. Furuno, H. Oshima, N. Kobayashi, T. Shimizu, H. Wang, H. Yoshikawa, *ACS Appl. Energy Mater.* **2025**, *8*, 12019.
[52] X.-Y. Gao, Y.-L. Li, T.-F. Liu, X.-S. Huang, R. Cao, *CrystEngComm* **2021**, *23*, 4743.

Batteries & Supercaps

Research Article
doi.org/10.1002/batt.202500524

Chemistry Europe
European Chemical
Societies Publishing

[53] A. Jouhara, E. Quarez, F. Dolhem, M. Armand, N. Dupré, P. Poizot, *Angew. Chem. Int. Ed.* **2019**, *58*, 15680.

[54] H.-H. Zong, C. Yao, C.-Q. Sun, J.-G. Zhang, L. Zhang, *Molecules* **2020**, *25*, 3232.

[55] H. Sano, A. Yoshimura, L. Zhang, H. Ebisawa, T. Kiyokawa, K. Fujita, Y. Misaki, M. Yao, *ACS Appl. Polym. Mater.* **2024**, *6*, 7542.

[56] M. Chen, L. Liu, P. Zhang, H. Chen, *RSC Adv.* **2021**, *11*, 24429.

[57] F. Wang, J. Wang, G. Li, Z. Guo, J. Chu, X. Ai, Z. Song, *Energy Storage Mater.* **2022**, *50*, 658.

[58] Y. Cho, D. Jang, J.-J. Park, H. Kye, J. E. Kwon, B.-G. Kim, *ACS Appl. Energy Mater.* **2024**, *7*, 7615.

[59] Y. Ham, C. Kim, D. Shin, I.-D. Kim, K. Kang, Y. Jung, D. Lee, S. Jeon, *Small* **2023**, *19*, 2303432.

[60] Y. Ham, N. J. Fritz, G. Hyun, Y. B. Lee, J. S. Nam, I.-D. Kim, P. V. Braun, S. Jeon, *Energy Environ. Sci.* **2021**, *14*, 5894.

[61] D. Kang, S. Sardar, R. Zhang, H. Noam, J. Chen, L. Ma, W. Liang, C. Shi, J. P. Lemmon, *Energy Storage Mater.* **2020**, *27*, 69.

[62] Y. Kawasaki, R. Sakakibara, M. Fujisaki, M. Yamashita, A. Yoshimura, T. Shirahata, M. Yao, Y. Misaki, *Bull. Chem. Soc. Jpn.* **2021**, *94*, 1059.

[63] A. Yoshimura, M. Yoshinouchi, K. Hemmi, Y. Aso, R. Utsumi, T. Shirahata, M. Yao, Y. Misaki, *New J. Chem.* **2023**, *47*, 11760.

[64] T. Shimizu, K. Wakamatsu, Y. Yamada, Y. Toyoda, S. Akine, K. Yoza, H. Yoshikawa, *ACS Appl. Mater. Interfaces* **2021**, *13*, 40612.

[65] B. E. Gurkan, Z. Qiang, Y.-M. Chen, Y. Zhu, B. D. Vogt, *J. Electrochem. Soc.* **2017**, *164*, H5093.

[66] X. Wang, X. Tang, P. Zhang, Y. Wang, D. Gao, J. Liu, K. Hui, Y. Wang, X. Dong, T. Hattori, A. Sano-Furukawa, K. Ikeda, P. Miao, X. Lin, M. Tang, Z. Zuo, H. Zheng, K. Li, H.-k. Mao, *J. Phys. Chem. Lett.* **2021**, *12*, 12055.

[67] I. Obraztsov, A. Bakandritsos, V. Šedajová, R. Langer, P. Jakubec, G. Zoppellaro, M. Pykal, V. Presser, M. Otyepka, R. Zbořil, *Adv. Energy Mater.* **2022**, *12*, 2103010.

[68] C. Ma, X. Zhao, L. Kang, K.-X. Wang, J.-S. Chen, W. Zhang, J. Liu, *Angew. Chem. Int. Ed.* **2018**, *130*, 9003.

[69] S. Wang, L. Wang, K. Zhang, Z. Zhu, Z. Tao, J. Chen, *Nano Lett.* **2013**, *13*, 4404.

[70] H. D. B. Jenkins, K.-P. Thakur, *J. Chem. Educ.* **1979**, *56*, 576.

[71] P. F. Lang, B. C. Smith, *Phys. Chem. Chem. Phys.* **2015**, *17*, 3355.

[72] T. L. Kulova, A. M. Skundin, *Energies* **2022**, *15*, 8615.

[73] C. Bao, B. Wang, P. Liu, H. Wu, Y. Zhou, D. Wang, H. Liu, S. Dou, *Adv. Funct. Mater.* **2020**, *30*, 2004891.

[74] X.-B. Cheng, R. Zhang, C.-Z. Zhao, Q. Zhang, *Chem. Rev.* **2017**, *117*, 10403.

[75] D. I. Iermakova, R. Dugas, M. R. Palacín, A. Ponrouch, *J. Electrochem. Soc.* **2015**, *162*, A7060.

[76] Z. Hua, *Appl. Comput. Eng.* **2023**, *26*, 233.

[77] P. K. Nayak, L. Yang, W. Brehm, P. Adelhelm, *Angew. Chem. Int. Ed.* **2018**, *57*, 102.

[78] B. L. Wittkamp, S. B. Hawthorne, D. C. Tilotta, *Anal. Chem.* **1997**, *69*, 1197.

[79] G. Zhao, K. Feng, *Water Environ. Res.* **2025**, *97*, e70022.

[80] K. Wakamatsu, A. Sekihara, Y. Yamaguchi, R. Matsushima, D. Matsumura, T. Kuila, H. Yoshikawa, *Batteries Supercaps* **2022**, *6*, e202200385.

[81] Y. Mitamura, H. Yorimitsu, K. Oshima, A. Osuka, *Chem. Sci.* **2011**, *2*, 2017.

[82] T.-C. Narayan, T. Miyakai, S. Seki, M. Dincă, *J. Am. Chem. Soc.* **2012**, *134*, 12932.